Hooker John, Noel (Orcid ID: 0000-0002-4129-6755)

Ruhl Micha (Orcid ID: 0000-0001-8170-0399)

Dickson Alexander (Orcid ID: 0000-0001-8928-4799)

Hansen Lars (Orcid ID: 0000-0001-6212-1842)

Shale anisotropy and natural hydraulic fracture propagation: An example from the Jurassic (Toarcian) Posidonienschiefer, Germany

John N. Hooker[1,2]

Micha Ruhl[1,3]

Alexander J. Dickson[1,4]

Lars N. Hansen[1]

Erdem Idiz[1]

Stephen P. Hesselbo[5]

Joe Cartwright[1]

[1]Department of Earth Sciences, University of Oxford, South Parks Road, Oxford, OX1 3AN, UK

[2]Department of Geosciences, Penn State University, 503 Deike Building, University Park, Pennsylvania 16802, USA

[3] Irish Centre for Research in Applied Geosciences (iCRAG) & Department of Geology, Trinity College Dublin, The University of Dublin, Dublin 2, Dublin, Ireland

[4]Department of Earth Sciences, Royal Holloway University of London, Egham, Surrey, TW20 0EX, UK

[5]Camborne School of Mines and Environment and Sustainability Institute, University of Exeter, Penryn Campus, Penryn, Cornwall, TR10 9FE, UK

Corresponding author: John Hooker (jzh497@psu.edu)

Key Points:

- Natural layer-parallel fractures in the Posidonienschiefer of Germany were driven open by fluid overpressures related to hydrocarbon maturation.
- Although these fractures lie at low angle to bedding, they propagated by steps that lie along bedding planes.
- Compared to fracture propagation via creation of two parallel fracture walls, this type of fracturing generates more surface area, and so is more stable.

Abstract

Cores recovered from the Jurassic (Toarcian) Posidonienschiefer (Posidonia Shale) in the Lower Saxony Basin, Germany, contain calcite filled fractures (veins) at low angle to bedding. The veins preferentially form where the shale is both organic rich and thermally mature, supporting previous interpretations that the veins formed as hydraulic fractures in response to volumetric expansion of organic material during catagenesis. Despite the presence of hydrocarbons during fracturing, the calcite fill is fibrous and so the veins appear to have contained a mineral-saturated aqueous solution as they formed. The veins also contain myriad host-rock inclusions having sub-millimetric spacing. These inclusions are strands of host rock that were entrained as the veins grew by separating the host rock along bedding planes, rather than cutting across planes. The veins therefore produce significantly more surface area—by a factor of roughly five, for the size of veins observed—compared to an inclusion-free fracture of the same size. Analysis of vein geometry indicates that, with propagation, fracture surface area increases with fracture length raised to a power between 1 and 2, assuming linear aperture-length scaling. As such, this type of fracture efficiently dissipates elastic strain energy as it lengthens, stabilizing propagation and precluding dynamic crack growth. The apparent separation of the host rock along bedding planes

suggests that the mechanical weakness of bedding planes is the cause of this inherently stable style of propagation.

Plain Language Summary

Natural fractures in rock give clues to how artificial fractures are likely to form and grow. This process is particularly important in shales, which have low permeability and tend to split along bedding planes. Shales therefore are often viewed as potential targets for top-seals, underneath which hydrocarbons may naturally accumulate, and CO_2 or wastewater may be stored. The fracturability of shales limits their effectiveness as top seals. In this paper we document natural fractures that propagated in shales and were affected by the mechanical weakness of shale bedding planes. We present a theoretical argument that the tendency of fractures to follow bedding planes in shales stabilizes fracture propagation. We conclude that mechanical anisotropy makes shales better top seals than is generally assumed based on rock fracture strength alone.

1 Introduction

Hydraulic fracturing in shale is important for the sealing capacity of shale layers during natural (Petrie et al., 2014; Foschi et al., 2018) and artificial (Elkhoury et al., 2015) fluid-expulsion events. The mechanical anisotropy of shale is evident from its fissility in hand samples, from abundant examples of layer-parallel natural fractures hosted in shales worldwide (Cobbold et al., 2013; Gale et al., 2014; Hooker et al., 2019), and from laboratory

experiments indicating that shale has a lower surface energy along bedding planes than across them (Chandler et al., 2016; Luo et al., 2018). This anisotropy could therefore guide fracture propagation into a layer-parallel orientation, improving the effective sealing capacity of shales. This process may be most pronounced for fluid-driven fractures, where high fluid pressures produce low effective stresses and theoretically low differential stresses, due to poroelastic stress coupling (Engelder & Fischer, 1994). Therefore, if imposed differential stresses, for example from tectonic loads, are small, then the relative importance of rock anisotropy is greater in determining the direction and extent of fracture propagation.

However, in most cases it is not clear what the past loading conditions were that led to fracturing (Laubach et al., 2019). Subsurface fracturing is theoretically driven by decreases in effective compression (e.g., Gudmundsson, 2011). In shales, such stress changes may be related to tectonic strains (Pireh et al., 2015; Ghosh et al., 2018), fluid overpressures (Zhang et al., 2016; Meng et al., 2017), diagenetic reactions (Hooker et al., 2017a), exhumation (Engelder & Gross, 2018), or thermal stresses (English, 2012). Consequently, there is very little constraint on the relative importance of mechanical anisotropy, high fluid pressures, or high horizontal loads for the growth of layer-parallel fractures. Nor is it easy to assess how mechanical anisotropy affects the dynamics of crack propagation, because of poor constraints on how fracture opening and propagation affect the effective stresses in the vicinity of fractures, through their effects on fluid pressure (Olson, 2003; McDermott et al., 2013; Mohammadnejad & Khoei, 2013).

The purpose of this paper is to examine the effects of shale anisotropy on natural hydraulic fractures. We take advantage of the circumstances regarding the formation of a particular set of fractures intersected by cores through the Lower Jurassic (Toarcian) Posidonienschiefer, in

the Lower Saxony Basin (LSB), Germany. New observations support a previous study (Jochum et al., 1995) suggesting that the fractures formed in response to fluid overpressures that arose from the maturation of organic matter. It is commonly interpreted that hydraulic fracturing in organic-rich shales forms veins and unmineralized mode 1 fractures as a direct result of volume change reactions during catagenesis, which have the effect of increasing local fluid pressures (e.g., Mandl & Harkness, 1987; Lash & Engelder, 2005). The four studied cores, from across the Posidonienschiefer in the LSB, are ideally located to test this hypothesis, because they represent a gradation in thermal maturity of the organic matter, from immature to highly mature, with vitrinite reflectance (VR) values from 0.5 to >3.

Furthermore, the fibrous mineral fill of the studied veins preserves information about opening kinematics, allowing us to interpret how the veins grew. The present veins dip obliquely with respect to bedding, but fibrous calcite cement deposits show that the veins propagated in *en échelon* steps, each of which split the rock along bedding planes. Therefore these natural hydraulic fractures illustrate the stabilizing effect of bedding-plane weakness on hydraulic fracture propagation.

2 Geologic Setting

The LSB (Figure 1a) is part of the Central European Basin System, which began as a foreland basin to the Variscan orogeny (Betz et al., 1987). The breakup of Pangea in the Late Triassic and Early Jurassic brought rifting and increased accommodation in the LSB (Kockel et al., 1994), primarily via extension along WNW striking normal faults (Betz et al., 1987). The Posidonienschiefer was deposited, at least in part, during the Toarcian Oceanic Anoxic Event

(T-OAE), a period of widespread anoxic–euxinic conditions in marginal marine environments across both hemispheres (Al-Suwaidi et al., 2016; Dickson et al., 2017; Them II et al., 2017), particularly in the northwest continental European Seaway, including the LSB (Jenkyns, 1988, 2010). High organic matter sequestration and associated high sedimentary total organic carbon (TOC) values formed in geo- and hydrographically restricted basins, under anoxic–euxinic water column conditions (Jenkyns, 1988).

During the Late Jurassic and Early Cretaceous, relatively rapid subsidence in the LSB resulted in the preservation of a thick, lacustrine-marine succession (Bruns et al., 2013). The Alpine orogeny in the Late Cretaceous reactivated pre-existing normal faults in a reverse sense, producing inversion structures, such that exhumation was widespread and to greatest extent within grabens (Bruns et al., 2013).

The localities of the cores used in this study lie within 200 km west of Hanover, Germany (Figure 1). The Posidonienschiefer in the studied cores lies at present-day depths between 1200 and 3500 m (Table 1). Maximum (pre-inversion) burial depths were estimated from basin modeling by Bruns et al. (2013) and are reported in Table 1. Regional seismic data (Baldschun et al., 1996) imaged numerous faults, including major graben-bounding faults (Figure 1b) that were reactivated during basin inversion.

The Lower Toarcian Posidonienschiefer in the LSB is informally referred to as the Lias Epsilon (e.g., Küspert, 1982), and is under- and overlain by the Lias Delta (Pliensbachian) and Lias Zeta (Upper Toarcian or Aalenian), respectively (Littke et al., 1991). The Lias Epsilon in the LSB is identified by its elevated TOC and calcite concentrations, such that its exact chronostratigraphic position may vary locally.

3 Methods

Fractures were identified in core as any planar discontinuities containing minerals, slickensides, or organic matter as evidence of formation in the subsurface. Cores tend to break apart along bedding planes, and there are also occasional breaks at high angle to bedding, often with irregular (non-planar) attitudes. Breaks of any orientation that lack minerals or slickensides as evidence of formation in the subsurface are attributed to coring or handling, and ignored in this study. Fractures filled or mostly filled by cement are termed veins. Fracture size and position were measured from core photographs, with calibration from physical core observation using a hand lens. For opening-mode fractures, which lack evidence of significant shear displacement, kinematic aperture was recorded in the sense of Marrett et al. (1999) as the total distance between separated fracture walls, regardless of whether the intervening space contains minerals or porosity.

This study focuses on calcite-filled veins, whose fibrous fill (see below) preserves mm-scale opening displacements. For such veins we therefore use the width of calcite cement to reflect the fracture kinematic aperture. This approach may underestimate the true original opening distance of veins if there were any collapse, pressure solution, or other processes that shrunk the veins after their formation. The approach may overestimate the true opening width if expansion during natural exhumation or coring and sampling occurred. However, the core- and petrographic-scale evidence presented below shows mostly intact veins without significant crystal or wall-rock deformation, except that due to the vein opening itself. Therefore, we estimate the error of our size measurements to be ±0.5 mm, based on our image pixel size. Fracture length was measured where two opposite fracture tips were preserved in core. Only small shear offsets were noted along fractures, as described below.

Cores were sampled for petrographic observation and geochemical analysis. Petrographic samples were cut into thin sections or polished core slabs. Samples were imaged using an FEI Quanta 650 scanning electron microscope at the Department of Earth Sciences, University of Oxford, using a 20 kV beam and 10 mm working distance. Crystallographic axes were mapped using an electron backscatter detector attached to the SEM. Total organic carbon (TOC) was quantified using a Rock Eval VI pyrolysis instrument, also at the Department of Earth Sciences, University of Oxford, following the methods in Behar et al. (2001).

4 Results

4.1 Lithology

Cores 1–3 preserve approximately 50 m of gray-brown to black mudrock with intercalated, commonly nodular, limestones (Figure 2). The bottom 2–5 m of this interval in each core contains unfractured, homogeneous mudrock; above this interval limestones alternate with shale. The limestones have thicknesses of several cm to 1 – 2 dm, commonly with gradational boundaries and nodular (ellipsoidal) to tabular morphologies. Here, the term shale denotes mudrock having a distinct bedding-parallel fabric of varying clay, calcite and organic matter composition. The cores tend to break along the sedimentary fabric, and abundant calcite veins lie at low angle to the shale bedding orientation (Figure 3a).

The lowest preserved limestone layers in the studied intervals of each core are coincident with the onset of TOC-enrichment (Figure 2) at the base of the Posidonienschiefer. Elevated TOC values are generally below 2% in the Lias Delta (below the Posidonienschiefer) and commonly increase to 10–15% in the Lias Epsilon. Within the high-TOC interval, the organic carbon content is generally lower in the limestone intervals than in the shale intervals. Moving upsection, limestones become sparser and are progressively more laminated and less nodular over several meters. Here laminae denotes mm-scale layers that are compositionally distinct, primarily by their carbonate mineral content, such that limestone and shale laminae commonly alternate to form cm- to dm-scale composite sequences (Figure 3c). Calcareous laminae and TOC both diminish upward, and the change is generally gradual (Figure 2). Core 4 preserves only the section from the top of the Posidonienschiefer down to the laminated interval.

The major sedimentary mineral constituents of the shale layers (Figure 3b) are clay, dominantly illite with locally abundant kaolinite (30–60% total), quartz grains and cement (10–20%), calcite cement (5–20%), calcitic microfossils, dominantly coccoliths (up to 20%), dolomite rhombohedra (up to 20%), pyrite, which is generally framboidal but may be pore-filling or -expanding (up to 20%), and apatite (up to 5%). TOC ranges from <1 to 18% (Figure 2). Laminated and nodular limestone layers contain greater abundances of calcite, both cements and fossils, relative to shale layers, generally at the expense of clay. The top of the organic-rich interval is sharp in Core 1, and more gradational in Cores 2 and 3, but within dark mudrock and not marked by any obvious lithological change in any core. Within the organic-rich section in the latter two cores, carbonate content is reflected in core color, with paler intervals richer in carbonate and poorer in organic matter and clay.

Shale layers within the high-TOC intervals in Cores 2 and 3 contain abundant layer-parallel calcite veins (Table 1). We have no TOC measurements from Core 4, but that core also has abundant veins in equivalent strata, using carbonate beds as correlation markers. Layer-parallel calcite veins are absent in the limestone and calcareous shale layers, and in the low-TOC mudstones of the Lias Delta, underlying the Posidonienschiefer. Shale layers containing layer-parallel veins are not compositionally laminated; however, the long axes of grains in these layers are strongly aligned in a horizontal attitude (Figure 3b, 4a).

4.2 Calcite veins

Layer-parallel vein morphologies vary by the angle of the face on which the vein is slabbed (observed). Because the cores are not oriented, the true orientation of any such face is unconstrained. However, individual veins observed on orthogonal cut faces commonly show a characteristic host-rock inclusion pattern on at least one such face. This pattern is a sigmoidal to parallelogram-shaped array of sub-millimetric vein segments, here termed *veinlets* (Figure 4a–d). The veinlets are thickest, vertically, near the center of the macroscopic vein and thinner toward the tips. Veinlets have close to constant horizontal thickness throughout the vein, and are separated by host-rock inclusions of near-constant, sub-millimetric thickness, along each inclusion and across the vein.

Vein walls generally make an angle of 10–20° from bedding. Away from the veins, the host-rock grains lie parallel to bedding. Where host-rock is included within the veins, the grains lie parallel to the inclusion (Figure 5a,b). Core faces cut vertically but parallel to veinlets show host-rock inclusions in vertical, U-shaped, and V-shaped arrays (Figure 4d).

Veins are filled by fibrous calcite, with trace pyrite crystals. In some instances, vein-like cements are entirely made up of pyrite (Figure 4c–f). Calcite crystals are long compared to their width and emanate from a median line (Bons et al., 2012) near the center of veins. Median lines appear discrete at the core-sample scale (Figure 4c, 4d), but are revealed to consist of myriad blocky crystals with host-rock inclusions intervening in various orientations (Figure 5c). Median lines lie oblique to both the vein walls and to bedding. Median lines appear to intersect or merge with either vein wall at a point inward of either tip (Figure 4c, d). Within each veinlet, the median line is roughly equidistant from either wall only near the vein center. Toward the upper vein tip, the median line is offset toward the bottom vein wall (Figure 5a); toward the lower tip, the median line is offset toward the top vein wall.

The longest dimension of the fibers is roughly perpendicular to the median line within each veinlet, and thus at an oblique angle to bedding. Fibers are rooted at the median lines within each veinlet (Figure 5). Away from the median lines, crystals become coarser and more equant, particularly toward the narrow ends of the sigmoidal veinlets. Electron backscatter diffraction mapping shows no crystallographic preferred orientation, either among crystals within the median line or among the fibers (Figure 5c).

Vein kinematic aperture ranges from ~0.1 to 13 mm (average 2.7 mm, standard deviation 1.8 mm). Veins do not appear to be associated with a significant microscopic-fracture population; no calcite veins were observed to be significantly thinner than the typical thickness of median lines, which is on the order of 0.1 mm (Figure 5b). The maximum tip-to-tip length we observed in core is 72 mm, owing to the 70 mm core width. The maximum aperture observed among small-length veins fully contained within core samples is 4 mm (Figure 6a). Among

these small veins there is a significant, positive correlation between kinematic aperture and length (p < 0.01 based on Pearson's r for linear, exponential, and power-law best fits). The data are insufficient to interpret a linear or sub-linear (power law) relationship between aperture and length; neither linear nor sub-linear best-fit equations between vein length and aperture can be rejected using chi-squared tests.

Consistent with a characteristic veinlet width, the number of veinlets per vein, measured from core observation, varies linearly with total vein length (Figure 6b). We observe 1.7 veinlets/mm of vein length (standard deviation 0.2 veinlets/mm). We estimate the uncertainty in veinlet counting at 20%, based on subjectivity of host-rock-strand continuity (Figure 4,5).

Overall layer-parallel vein abundance varies from 0.5 to 19 m^{-1} within the Lias Epsilon (high TOC) interval (Table 1). Core 1 has the lowest abundance of layer-parallel veins (Table 1). Core 2 has intermediate vein abundance, and Cores 3 and 4 have the highest vein abundance (Table 1). Moreover, analyzing Cores 2 and 3 individually, vein abundance correlates very closely with the TOC in the host rock (Figure 2). Layer parallel veins are virtually absent away from high-TOC intervals.

4.3 Thermal maturity and depth of burial

Rock Eval data (Figure 2, Table 1) are consistent with previous maximum paleodepth estimates based on vitrinite reflectance and other temperature indicators (Bruns et al., 2013) suggesting that thermal maturity varies considerably across the study area. Core 1 is immature and Cores 2 and 3 are considerably more mature, having hydrogen indices reduced

to nearly zero (Table 1). No thermal maturity data are available from Core 4, but its geographic proximity to Core 3 (Figure 1b) is consistent with a high thermal maturity as well.

The distance between each core site and the closest seismically resolvable fault (Baldschun et al., 1996) is also illustrated in Figure 1b. These were interpreted as inverted normal faults separating regions of strongly disparate maximum burial (Bruns et al., 2013). The degree of exhumation for Cores 2, 3, and 4 is estimated to be on the order of 3000 m, based on modeled maximum burial depths (Bruns et al., 2013) and the present-day core interval depth (Table 1). These cores were drilled through the same basin-scale graben (Figure 1b); Core 2 was drilled closer to the southern margin, 10 km from the southern fault; Cores 3 and 4 were drilled close to the center, roughly 20 km from either fault. Core 1 is estimated to have undergone a much shallower maximum burial and exhumation of less than 100 m (Table 1); this core was drilled through the footwall of the normal fault bounding this graben to the north, at a distance of roughly 10 km from the fault (Figure 1).

5 Discussion

5.1 Hydrocarbon maturation as vein formation mechanism

The observed intensity of veins within the high-TOC interval (Figure 2, Table 1) is not correlated to fault proximity. In previous studies, fracture intensity has been shown to increase near larger-scales structures such as buttress anticlines (e.g., Glen et al., 2005) and otherwise isolated faults (Laubach et al., 2014). Such fault-zone fractures are interpreted as a manifestation of progressive brittle strain during fault slip (Laubach et al., 2014; Ferrill et al.,

2019). In the present cores, however, the veins are not systematically distributed around the seismically resolvable, graben-bounding faults, nor are there appreciable changes in bedding attitude within the fractured core intervals. We therefore find little evidence that the veins represent fault-zone damage.

Rather, there is a strong correlation between organic matter, thermal maturity, and layer-parallel fracturing (Figure 2, Table 1). Variation in maturity throughout the study area is thought to reflect variation in thermal exposure, and is likely linked to structural position: the WNW-striking normal faults produced a horst and graben architecture to the basin prior to inversion during the Late Cretaceous (Bruns et al., 2013), with downthrown fault blocks buried to a significantly greater depth than adjacent blocks. As organic rich rocks mature, the degree of conversion of the original kerogen to petroleum–bitumen products also increases. If the expulsion of the petroleum products had been hindered by the generally low permeability of the host source-rock, it is possible that the intensity of the hydraulic fracturing driven by the maturation process would also have increased (see Mandl & Harkness, 1987). A low-permeability, generally closed fluid system is also consistent with previous laboratory studies of shales (Neuzil, 1994) and with the vein fills comprising minerals that are also abundant within the host rock (Hooker et al., 2017b). Our observations therefore support those of Jochum et al. (1995) that layer parallel veins were formed by volume increase and overpressure related to the maturation of organic matter; i.e. the veins are natural hydrofractures driven by catagenesis.

5.2 Growth of sigmoidal veinlets

5.2.1 Antitaxial cementation

In general, veins comprising a median line surrounded by continuous, fibrous fill that extends to the vein walls are interpreted to have filled antitaxially (Bons et al., 2012). That is, such veins originate as thin veins at the median line and then simultaneously widen and fill by adding cement at the vein-wall interface.

Previous numerical models have recreated this antitaxial texture by assuming that crystals at the median line have random crystallographic orientations (Hilgers et al., 2001; Ankit et al., 2015). These models then posit that cementation occurs by epitaxial overgrowth of these randomly oriented seed crystals, such that crystal growth passively fills in the space between the fiber tip and the vein wall. Accordingly, if the walls of a growing vein move apart slowly enough, each crystal will be able to grow fast enough to fill that ephemeral space, regardless of crystallographic orientation, and fibrous fill will result. In contrast, if the vein opening rate is faster, only those crystals having fast growth axes at high angle to the vein wall will keep up with the opening rate, and a coarser fill style will develop, which also has a crystallographically preferred orientation (Hilgers et al., 2001; Ankit et al., 2015; Lander & Laubach, 2015).

The fibrous texture of the vein fill observed here, combined with the lack of crystallographic preferred orientation, therefore supports previous models of cement fill, where cementation was simultaneous with, and at the same rate as, vein opening. The vein opening rate was presumably a function of the vein driving stress, which in this case was the sum of the overburden and the internal hydrocarbon fluid pressure.

5.2.2 Nature of host-rock strands

The veins include myriad strands of host rock. Two competing interpretations of these strands are that they are inclusions, which were incorporated into the veins during vein growth, or alternatively, that they are the result of fracturing of initially continuous calcite veins. We prefer the former interpretation, for two reasons.

First, the long axes of grains within the host rock, away from fractures, tend to lie parallel to bedding, whereas within host-rock strands, grain long-axes are rotated toward parallel with the strands (Figure 5a,b). Thus it appears that the sedimentary fabric was rotated within tilted host-rock strands, as opposed to being cleft or truncated by veinlets, or sheared as a result of injection between veinlets. The rotation of the host-rock fabric is consistent with inclusion of host-rock between veinlets that grow against one another while propagating along, and not across, bedding planes.

Second, the host-rock strands delineate the boundaries between calcite crystal domains that are undeformed and have contrasting textures and crystallographic axis orientations. Figure 5c shows that fibers commonly terminate not against the outer vein wall but against host-rock inclusions between the median line and the outer wall. Within the tips of veinlets, outward of host-rock inclusions, the vein fill becomes coarser. If the veins were composed of continuous, fibrous calcite before introduction of host-rock strands, then we would expect general continuity of fibers on either side of those strands. Fibers could be rotated during a hypothetical shearing episode, but we see no significant deviation of the attitude of fibers throughout the veins. Nor do we see deformation of crystal lattices, which would be marked by changes of crystallographic orientation within individual crystals.

The absence of fibers within the narrow ends of the veinlets (Figure 5c) suggests that continued growth (opening and propagation) of the veinlets was filled by cements overgrowing progressively coarser substrates toward the veinlet tips. As with fibers, we might expect to see crystallographically parallel blocky crystals across host-rock strands, if those strands formed by the fracturing of previously continuous calcite crystals. And although some crystals on either side of strands have similar crystallographic orientations (Figure 5c), there are abundant examples of highly contrasting orientations across even relatively thin strands, judging by the inverse pole figure (color key, Figure 5c). This observation favors the interpretation that the host-rock strands were incorporated between originally distinct calcite crystals, rather than having been translated in among previously continuous calcite crystals.

Networks of host-rock strands amid vein-like calcite aggregates are also present in cone-in-cone structure (e.g., Cobbold et al., 2013). Analogous observations—namely, highly contrasting crystallographic orientations between undeformed crystals separated by thin host-material strands—were used to argue for incorporation of host sediment (Maher et al., 2017) or host rock (Hooker & Cartwright, 2018) during cone-in-cone growth, and not afterward.

5.2.3 Growth reconstruction

To understand how these veins formed, and the role of shale mechanical anisotropy in their development, we present a growth reconstruction model (Figure 7) that accounts for several key observations. These include (i) the antitaxial formation and (ii) syn-growth incorporation of host rock strands mentioned above, as well as (iii) positively correlated aperture and length (Figure 6), (iv) veinlets that propagate along bedding planes and not across them (Figure 5b),

(v) median lines that lie oblique to both bedding and the vein long dimension (Figure 4c,d), and (vi) a characteristic veinlet width, which does not systematically vary with position inside veins or with vein size (Figure 4).

We interpret that veins in the Posidonienschiefer of the LSB initiated as single veinlets, which separated the host rock at a location now marked by the median line of the center-most veinlet (Figure 7). The initial veinlet widened and lengthened along the same bedding plane, filling with fibrous calcite as it grew. But, owing to non-parallelism between the applied stress field and the sedimentary fabric, the vein propagation direction was oblique to bedding. After some enlargement, rather than cutting across bedding planes, a new veinlet (veinlet 2 in Figure 7) formed near either tip of the original veinlet, beginning an *en échelon* array.

The vein continued to lengthen in the same manner, with a new veinlet added at either tip once the preceding tip-veinlets reached a certain size. This addition of new veinlets resulted in a regular spacing of veinlets as the vein grew (Figure 7). The earlier-formed veinlets continued to widen as the veins grew; widening was accomplished by progressive separation of the host rock along bedding; i.e. by propagation such that the outer veinlet wall remained parallel to the sedimentary fabric, and such that the internal, dipping veinlet wall remained parallel to the sedimentary grain within the rotated host-rock strand. Note that the marker horizons in Figure 7 are continually entrained between the same veinlet pair as the vein grows.

In order to illustrate the veinlet-scale growth of veins in Figure 7, we simplify the median line as a discrete surface through the center of the vein. SEM images (Figure 5a-c) show that the median line is actually a zone of microscopically blocky crystals having myriad tiny host-

rock strands included among them. A subset of these inclusions extend to the outer vein wall, forming the veinlet boundaries. Marker horizons in the figure are drawn so as to conserve length, to bend within the vein's host-rock inclusions, and to lie horizontal away from the vein. This approach illustrates the mixed kinematics (opening plus left-lateral shear, as drawn) inferred from the geometry of the crystals and host-rock inclusions. However, the true strain distribution around the veins is unclear, owing in part the to the homogeneity of the host sediment. The true displacement field around the veins is likely compensated, to a large extent, by nearby veins.

We suggest that the veinlets in Figure 7 are longer and blade-shaped in the third dimension, into the page. This would account for the long, continuous shape of vein segments in orthogonal cut faces (Figure 3b, smaller fractures in Figure 3a, 4e-f).

A potential alternative reconstruction-model might hold that each macroscopic vein formed by the initial development of an array of uncemented microfractures, which variably grew taller in a second phase of calcite precipitation-related expansion. However, this interpretation is belied by the fact that longer, thicker veins have veinlet widths and spacings similar to those of small veins (Figure 4, 6b). If this pattern emerged from *en échelon* arrays of tiny fractures of equal length, with overall array-length a linear function of the number of tiny fractures present, then the final aperture of each calcite vein would seem to have been predestined by the number of tiny fractures in the array. For example, suppose there are two arrays of microfractures, alike in all respects except one is formed of 50 fractures and is 30 mm in total length, and the other is formed of 100 fractures and is 60 mm in total length. This alternative hypothesis would imply that once these arrays evolve into veins, the latter vein would have twice the final *aperture* of the former, because it had twice the initial *length*. In

contrast, by our model each vein grew by widening and adding new veinlets at its tips at regular intervals of growth, accounting for the observation of *more* veinlets within longer, thicker veins.

5.3 Vein mechanics

The interpretation of vein growth, detailed in the kinematic model outlined above, implies that weakness along the bedding fabric in shales can exert an important control on natural hydraulic fracture propagation. Ideally, opening-mode fractures propagate in a plane perpendicular to the minimum compressive stress direction (e.g., Cosgrove, 1995). Where this direction is misaligned with the pole to the bedding fabric, the fracture propagation path and total distance will reflect an energy minimization between the imposed stress field and the material weakness. Understanding this phenomenon will help to better predict the behavior of induced fractures in the subsurface.

To quantify the mechanical effects of shale laminae on fracture propagation, we begin by using an approach based on linear elastic fracture mechanics. We posit that the propagation of the macroscopic veins is analogous to that of natural fractures, based on (i) the crack-like geometry of macroscopic veins; (ii) hooking, branching, and *en échelon* stepping relationships between macroscopic veins; (iii) the presence of median lines; (iv) vein crystal fibers that are mutually parallel among the many veinlets, and perpendicular to median lines; and (v) their inferred fluid-overpressure opening mechanism.

Within an elastic rock body, the energy available to propagate a fracture, by creating fracture surface area A, comes from the elastic strain energy U stored within the rock (Gudmundsson, 2011). Neglecting energy losses in the form of heat, sound, or other kinetic forms, fracturing is the transformation of elastic strain energy into surface energy and any associated plastic deformation of the host. Assuming elastic behavior, the change in elastic strain energy as a result of fracture propagation (i.e., an increase in fracture surface area), is given by:

$$\Delta U = G\, \Delta A \qquad\qquad\qquad\qquad (1)$$

where $G = 2\gamma$ and γ is the surface energy of the rock. The factor of two accounts for fracture propagation creating two surfaces.

Griffith (1920) derived the magnitude of U_0, the amount of elastic strain energy diminished within an elastic body due to the presence of a fracture. The fracture is modeled as having an elliptical cross section whose half-length a is much larger than its half-aperture b; the fracture cuts a plate having infinite extent in the a-b plane and unit thickness. Assuming plane strain and uniaxial extension, the strain energy released from the unit-thickness plate is (e.g., Gudmundsson, 2011):

$$U_0 = [\sigma^2(1-v^2)/2E]\, \pi a^2 \qquad\qquad\qquad\qquad (2)$$

where σ is the remote applied stress from uniaxial extension, v is Poisson's ratio, and E is Young's modulus. As such, ΔU increases with a^2. Because the fracture surface area only increases linearly with a for opening-mode propagation, fracture propagation under a

constant load will progressively dissipate elastic strain energy faster than newly created

surface area absorbs surface energy, and so propagation will accelerate unstably.

Because the present fractures are actually arrays of veinlets, they generate considerably more

surface area per unit increase in a. We can estimate dA/da by representing the veinlets as

plane-strain fractures whose surface area, per unit thickness as in Griffith's scenario, is

$$A_{veinlet} = 2L \qquad\qquad (3)$$

where L is the length of a line transecting the macro-vein ellipse at a point along $[-a, a]$ and

lying at an angle θ (estimated at 70° for the calculations below) from the major axis (Figure

8). These veinlets are spaced at a constant interval distance S along the ellipse. Equation 3 is

a conservative estimation of the true surface area in that it ignores veinlet curvature in the a-b

plane, but the under-estimation will be small where b/S is large. As stated above, S is

observed to remain roughly constant through vein growth, so the degree of under-estimation

should diminish with vein growth. The total A for a macroscopic calcite vein is the

summation of Equation 3 across the vein:

$$A_{vein} = \sum_{n=1}^{2a/S} A_n \qquad\qquad (4)$$

Inspection of Figure 8 reveals that the increase in the total surface area (sum of all veinlet

surfaces) with a depends on the aspect ratio (b/a) taken on by the vein as it grows. We

assume that this relationship is linear or sublinear, based on veins of different final sizes, as

preserved in cores. For linear or sublinear scaling $b \propto a^n$ ($n \le 1$), A increases with a^{1+n}. As

such, for linear b:a scaling, A increases with a^2 (Figure 9). In such a case, even if the fracture

formed under a constant load, the dissipation of elastic strain energy as the fracture grew would be matched by the absorption of surface energy created by the fracture.

For sublinear *b:a* scaling, increased surface creation during lengthening would not be sufficient to result in stable propagation under constant-load conditions, but would nevertheless generate more surface area, compared to the case of an ellipsoidal crack. The best-fit power law to the observed data (Figure 6a) indicates *b* scaling with $a^{0.75}$—although the quality of this fit is statistically indistinguishable from that of the linear best-fit.

We observe fractures having *2a* as great as 72 mm; many veins are likely much longer but truncated by the core. At this observed length scale, and assuming linear *b:a* scaling, the observed veins have approximately five times as much surface area as an equivalently sized ellipsoidal fracture (Figure 9).

5.4 Implications

Natural hydraulic (fluid-pressure-driven) fractures probably do not propagate under constant loads. The source of pressurized fluid is finite, and fluid pressure probably cycled within fractures, transiently diminishing as fracture volume increased (Lacazette & Engelder, 1992). Therefore the driving stress for natural hydraulic fractures likely diminished over time, consistent with field evidence that fractures eventually arrest. This study documents a natural example wherein propagation along the mechanical anisotropy of shales resulted in excess fracture surface area with fracture growth. This result would have produced a stabilizing effect during fracture growth, as elastic strain energy was more quickly dissipated as surface

area, compared to the ideal case of two discrete fracture surfaces. We therefore conclude from this case study of the vein distribution, geometry, and structure in the Posidonienschiefer of the LSB, that excess surface area generation can serve as a potential stabilizer of natural hydraulic fracture propagation in shales.

Artificial hydraulic fracturing must take into account fracture propagation, whether as a desired result in hydrocarbon exploration, or as a hazard in wastewater or CO_2 storage. Laboratory studies of fracture propagation along bedding in shales suggest that the fracture toughness, which is proportional to the square root of surface energy, may be reduced to roughly half the value across bedding (Chandler et al., 2017; Luo et al., 2018). Pre-existing fractures are also planes of weakness that can deflect fracture paths (Lee et al., 2015). Sedimentary planes of weakness appear to be the reason for the stepwise propagation of the present veins. It remains to be seen under what conditions the stabilizing effect described above emerges during natural or artificial fracturing, but the necessary conditions would appear to include some mechanical anisotropy and a driving stress oriented oblique to it, promoting *en échelon* stepping across bedding planes.

The formation of the present fractures is attributed to fluid overpressure. Structures that are similar, in that they contain fibrous mineral fill and, in some cases, abundant host-shale inclusions (e.g., "beef" and "cone-in-cone") have also been attributed to fluid overpressures (Cobbold et al., 2013; Zanella et al., 2015; Zhang et al., 2016; Meng et al., 2017). In settings not conducive to calcite precipitation, this type of fracture propagation may be common, but simply not preserved. However, simultaneous calcite precipitation may have important effects on propagation. Olson (2003) suggested that hydraulic-fracture propagation might be stabilized by fracture lengthening being matched with narrowing in order to preserve fracture

volume, for cases in which infiltration of fluids is slow compared to fracture growth. In the case of fibrous veins, although there may be some small, transient fracture open space at the vein-wall interface (Hilgers et al., 2001), simultaneous cementation with fracture growth would prevent fracture closure, precluding closure as a potential stabilizing mechanism.

6 Conclusions

Layer-parallel calcite veins in the Posidonienschiefer of the Lower Saxony Basin, Germany, formed as natural hydraulic fractures in response to hydrocarbon maturation-related overpressure. The veins filled with calcite cement as they lengthened and widened. Macroscopically, they lie oblique to the shale bedding fabric; however, microscopic evidence shows that they propagated by stepping across bedding planes. In fact, essentially all fracture opening occurred along bedding planes. The fractures repeatedly entrained host-rock inclusions as they grew, creating excess surface area during growth, relative to the ideal case in which fractures make only two surfaces. This excess surface area generation would have produced a stabilizing effect, by which more elastic energy is consumed per unit increase in fracture length. Thus shale anisotropy could potentially stabilize hydraulic fracture propagation.

References

Al-Suwaidi, A.H., Hesselbo, S.P., Damborenea, S.E., Manceñido, M.O., Jenkyns, H.C., Riccardi, A.C., Angelozzi, G.N., & Baudin, F. (2016). The Toarcian Oceanic Anoxic Event (Early Jurassic) in the Neuquén Basin, Argentina: A Reassessment of Age and Carbon Isotope Stratigraphy. *The Journal of Geology*, 124(2), 171 – 193.

Ankit, K., Selzer, M., Hilgers, C., & Nestler, B. (2015). Phase-field modeling of fracture cementation processes in 3-D. *Journal of Petroleum Science Research*, 4(2), 79 – 96, doi: 10.1002/2017GC006888

Baldschun, R., Kockel, F., Best, G., Deneke, E., Frisch, U., Juergens, U., Schmitz, J., Sattler-Kosinowski, S., Stancu-Kristoff, G., & Zirngast, M. (1996). *Geotektonischer Atlas von NW-Deutschland/Tectonic Atlas of NW Germany* (scale 1:300,000). Bundesanstalt für Geowissenschaften und Rohstoffe, Hannover.

Behar, F., Beaumont, V., & Penteado, H.D.B. (2001). Rock Eval 6 technology: Performances and developments. *Oil & Gas Science and Technology*, 56(2), 111 – 134.

Betz, D., Fürher, F., Greiner, G., & Plein, E. (1987). Evolution of the Lower Saxony Basin. *Tectonophysics*, 137, 127 – 170.

Bons, P.D., Elburg, M.A., & Gomez-Rivas, E. (2012). A review of the formation of tectonic veins and their microstructures. *Journal of Structural Geology*, 43, 33 – 62.

Bruns, B., Di Primio, R., Berner, U., & Littke, R. (2013). Petroleum system evolution in the inverted Lower Saxony Basin, northwest Germany: a 3D basin modeling study. *Geofluids*, 13, 246 – 271.

Chandler, M.R., Meredith, P.G., Brantut, N., & Crawford, B.R. (2016). Fracture toughness anisotropy in shale. *Journal of Geophysical Research Solid Earth*, 121, 1706–1729.

Cobbold, P.R., Zanella, A., Rodrigues, N., & Løseth, H. (2013). Bedding-parallel fibrous veins (beef and cone-in-cone): Worldwide occurrence and possible significance in terms of fluid overpressure, hydrocarbon generation and mineralization. *Marine and Petroleum Geology*, 43, 1 – 20.

Cosgrove, J.W. (1995). The expression of hydraulic fracturing in rocks and sediments. In Ameen, M.S. (ed.) *Fractography: fracture topography as a tool in fracture mechanics and stress analysis. Geologicical Society, London, Special Publications* 92, 187 – 196. doi: 10.1144/GSL.SP.1995.092.01.10

Dickson, A.J., Gill, B.C., Ruhl, M., Jenkyns, H.C., Porclli, D., Idiz, E., Lyons, T.W., & van den Boorn, S.H.J.M. (2017). Molybdenum-isotope chemostratigraphy and paleoceanography of the Toarcian Oceanic Anoxic Event (Early Jurassic). *Paleoceanography and Paleoclimatology*, 32(8), 813 – 829.

Elkhoury, J.E., Detwiler, R.L., & Ameli, P. (2015), Can a fractured caprock self-heal? *Earth and Planetary Science Letters*, 417, 99 – 106.

Engelder, T. & Fischer, M.P. (1994). Influence of poroelastic behavior on the magnitude of minimum horizontal stress, S_h, in overpressured parts of sedimentary basins. *Geology*, 22, 949 – 952.

Engelder, T. & Gross, M. (2018). Pancake joints in Utica gas shale: Mechanisms for lifting overburden during exhumation. *Journal of Structural Geology*, 117, 241 – 250.

English, J.M. (2012). Thermomechanical origin of regional fracture systems. *AAPG Bulletin*, 96(9), 1597 – 1625.

Ferrill, D.A., Smart, K.J., & Morris, A.P. (2019). Fault failure modes, deformation mechanisms, dilation tendency, slip tendency, and conduits versus seals. *Geological Society, London, Special Publication,* 496, doi: 10.1144/SP496-2019-7.

Foschi, M., Cartwright, J., & MacMinn, C.W. (2018). Sequential vertical gas charge into multilayered sequences controlled by central conduits. *AAPG Bulletin*, 102(5), 855 – 883.

Gale, J.F.W., Laubach, S.E., Olson, J.E., Eichhubl, P., & Fall, A. (2014). Natural fractures in shale: A review and new observations. *AAPG Bulletin*, 98(11), 2165 – 2216.

Ghosh, S., Hooker, J.N., Bontempi, C.P., & Slatt, R.M., 2018. High-resolution stratigraphic characterization of natural fracture attributes in the Woodford Shale, Arbuckle Wilderness and US-77D outcrops, Murray County, Oklahoma. *Interpretation* 6(1), SC29 – SC41.

Glen, R.A., Hancock, P.L., & Whittaker, A. (2005). Basin inversion by distributed deformation: the southern margin of the Bristol Channel Basin, England. *Journal of Structural Geology*, 27, 2113 – 2134.

Griffith, A.A. (1920). The phenomena of rupture and flow in solids. *Philosophical Transactions of the Royal Society of London*, A221, 163 – 198.

Gudmundsson, A. (2011). *Rock Fractures in Geological Processes*. Cambridge: Cambridge University Press, 578 p.

Hilgers, C., Koeh, D., Bons, P.D., & Urai, J.L. (2001). Development of crystal morphology during unitaxial growth in a progressively widening vein: II. Numerical simulations of the evolution of antitaxial fibrous veins. *Journal of Structural Geology*, 23(6 – 7), 873 – 885.

Hooker, J.N. & Cartwright, J. (2018). Dolomite overgrowths suggest a primary origin of cone-in-cone. *Geological Magazine*, 155(3), 568–585. doi: 10.1017/S0016756816000807

Hooker, J.N., Huggett, J.M., Cartwright, J., & Ali Hussein, M. (2017a). Regional-scale development of opening-mode calcite veins due to silica diagenesis. *Geochemistry, Geophysics, Geosystems*, 18(7), 2580 – 2600. doi: 10.1002/2017GC006888

Hooker, J.N., Cartwright, J., Stephenson, B., Silver, C., Dickson, A.J., & Hsieh, Y.-T. (2017b). Fluid evolution in fracturing black shales, Appalachian Basin. *AAPG Bulletin* 101(8), 1203 – 1238.

Hooker, J.N., Abu-Mahfouz, I., Meng, Q., & Cartwright, J. (2019). Fractures in mudrocks: Advances in constraining timing and understanding mechanisms. *Journal of Structural Geology*, 25, 166 – 173. doi: 10.1016/j.jsg.2018.04.020

Jenkyns, H.C. (1988). The early Toarcian (Jurassic) anoxic event – stratigraphic, sedimentary, and geochemical evidence. *American Journal of Science*, 288(2), 101 – 151.

Jenkyns, H.C. (2010). Geochemistry of oceanic anoxic events. *Geochemistry, Geophysics, Geosystems*, 11(3), doi: 10.1029/2009GC002788

Jochum, J., Friedrich, G., Leythaeuser, D., Littke, R., & Ropertz, B. (1995). Hydrocarbon-bearing fluid inclusions in calcite-filled horizontal fractures from mature Posidonia Shale (Hils Syncline, NW Germany). *Ore Geology Reviews*, 9, 363 – 370.

Kockel, F., Wehner, H., & Gerling, P. (1994). Petroleum systems of the Lower Saxony Basin, Germany. In L.B. Magoon & D.G. Dow (Eds.), *The petroleum system—from source to trap, AAPG Memoir*, 60, 573 – 586.

Küspert, W. (1982). Environmental changes during oil shale deposition as deduced from stable isotope ratios. In G. Einsele & A. Seilacher (Eds.), *Cyclic and Event Stratification*. Berlin: Springer, 536 p.

Lacazette, A. & Engelder, T. (1992). Fluid-driven cyclic propagation of a joint in the Ithaca Siltstone, Appalachian Basin, New York. In B. Evans & T.-F. Wong (Eds.), *Fault Mechanics and Transport Properties of Rocks*. London: Academic Press, 524 p.

Lander, R.H. & Laubach, S.E. (2015). Insights into rates of fracture growth and sealing from a model for quartz cementation in fractured sandstones. *GSA Bulletin* 127 (3/4), 516 – 538. doi: 10.1130/B31092.1

Lash, G.G. & Engelder, T. (2005). An analysis of horizontal microcracking during catagenesis: Example from the Catskill delta complex. *AAPG Bulletin*, 89(11), 1433 – 1449.

Laubach, S.E., Lander, R.H., Criscenti, L.J., Anovitz, L.M., Urai, J.L., Pollyea, R.M., Hooker, J.N., Narr, W., Evans, M.A., Kerisit, S.N., Olson, J.E., Dewers, T., Fisher, D.M., Bodnar, R., Evans, B., Dove, P., Bonnell, L.M., Marder, M.P., & Pyrak-Nolte, L., 2019. The role of chemistry in fracture pattern development and opportunities to advance interpretations of geological materials. *Reviews of Geophysics* 57(3), 1065 – 1111. doi: 10.1029/2019RG000671.

Laubach, S.E., Eichhubl, P., Hargrove, P., Ellis, M.A., & Hooker, J.N. (2014). Fault core and damage zone fracture attributes vary along strike owing to interaction of fracture growth,

quartz accumulation, and differing sandstone composition. *Journal of Structural Geology*, 68, 207 – 226.

Lee, H.P., Olson, J.E., Holder, J., Gale, J.F.W., & Myers, R.D. (2015). The interaction of propagating opening mode fractures with preexisting discontinuities in shale. *Journal of Geophysical Research Solid Earth 120*, 169–181.

Littke, R., Baker, D.R., Leythaeuser, D., & Rullkötter, J., 1991. Keys to the depositional history of the Posidonia Shale (Toarcian) in the Hils Syncline, northern Germany. In Tyson, R.V. & Pearson, T.H. (Eds.), *Modern and Ancient Continental Shelf Anoxia: Geological Society, London, Special Publication,* 58, 311 – 333.

Luo, Y., Xie, H.P., Zhang, R., Li, C.B., & Gao, C. (2018). Mechanics characterization of an anisotropic shale. *Scientific Reports*, 8, article number 8505, DOI:10.1038/s41598-018-26846-y.

Maher, H.D., Jr., Ogata, K., & Braathen, A. (2017). Cone-in-cone and beef mineralization associated with Triassic growth basin faulting and shallow shale diagenesis, Edgeøya, Svalbard. *Geological Magazine,* 154(2), 201–216, doi:10.1017/S0016756815000886

Mandl, G. & Harkness, R.M. (1987). Hydrocarbon migration by hydraulic fracturing. In M.E. Jones & R.M.F. Preston (Eds.), *Deformation of Sediments and Sedimentary Rocks, Geological Society, London, Special Publications* 29, 39 – 53.

Marrett, R., Ortega, O.J., and Kelsey, C.M. (1999). Extent of power-law scaling for natural fractures in rock. *Geology* 27(9), 799 – 802.

McDermott, C.I., Edlmenn, K. & Haszeldine, R.S. (2013). Predicting hydraulic tensile fracture spacing in strata-bound systems. *International Journal of Rock Mechanics & Mining Sciences* 63, 39 – 49.

Meng, Q., Hooker, J.N., & Cartwright, J. (2017). Early overpressuring in organic-rich shales during burial: evidence from fibrous calcite veins in the Lower Jurassic Shales-With-Beef Member in the Wessex Basin, UK. *Journal of the Geological Society*, 174(5), 869 – 882.

Mohammadnejad, T. & Khoei, A.R. (2013). An extended finite element method for hydraulic fracture propagation in deformable porous media with the cohesive crack model. *Finite Elements in Analysis and Design* 72, 77 – 95.

Neuzil, C.E. (1994). How permeable are clays and shales? *Water Resources Research* 30(2), 145 – 150.

Olson, J.E. (2003). Sublinear scaling of fracture aperture versus length: An exception or the rule? *Journal of Geophysical Research*, 108(B9). doi: 10.1029/2001JB000419

Petrie, E.S., Evans, J.P., & Bauer, S.J. (2014). Failure of cap-rock seals as determined from mechanical stratigraphy, stress history, and tensile-failure analysis of exhumed analogs. *AAPG Bulletin*, 98(11), 2365 – 2389.

Pireh, A., Alavi, S.A., Ghassemi, M.R., & Shaban, A. (2015). Analysis of natural fractures and effect of deformation intensity on fracture density in Garau formation for shale gas development within two anticlines of Zagros fold and thrust belt, Iran. *Journal of Petroleum Science and Engineering*, 125, 162 – 180.

Them II, T.R., Gill, B.C., Caruthers, A.C., Gröcke, D.R., Tulsky, E.T., Martindale, R.C., Poulton, T.P., & Smith, P.L. (2017). High-resolution carbon isotope records of the Toarcian Oceanic Anoxic Event (Early Jurassic) from North America and implications for the global drivers of the Toarcian carbon cycle. *Earth and Planetary Science Letters*, 459, 118 – 126.

Zanella, A., Cobbold, P.R., & Boassen, T. (2015). Natural hydraulic fractures in the Wessex Basin, SW England: Widespread distribution, composition and history. *Marine and Petroleum Geology*, 68(A), 438 – 448.

Zhang, J., Jiang, Z., Jiang, X., Wang, S., Liang, C., & Wu, M. (2016). Oil generation induces sparry calcite formation in lacustrine mudrock, Eocene of East China. *Marine and Petroleum Geology*, 71, 344 – 359.

Table 1. Rock Eval data, fracture frequency, burial depths, and fault distances for Cores 1–4. Rock Eval data were not collected from Core 4.

	Hydrogen Index		Oxygen Index					
Core	Average	Std. Dev.	Average	Std. Dev.	Depth of high-TOC interval (present day) (m)	Estimated max burial depth * (m)	Layer-parallel fractures per m, within high-TOC interval	Distance to nearest mapped fault (km)†
1	589	155	21	36	1420-1453	1500	0.545	10.3
2	2	2	19	11	1238-1266	4300	8.89	10.0
3	3	4	13	4	3258-3290	6300	17.6	20.3
4					2584-2606**	5600	18.5	18.6

*Based on basin model of Bruns et al. (2013)

†Based on seismically detected faults (Baldschun et al., 1996)

** 2606 m is the bottom of Core 4
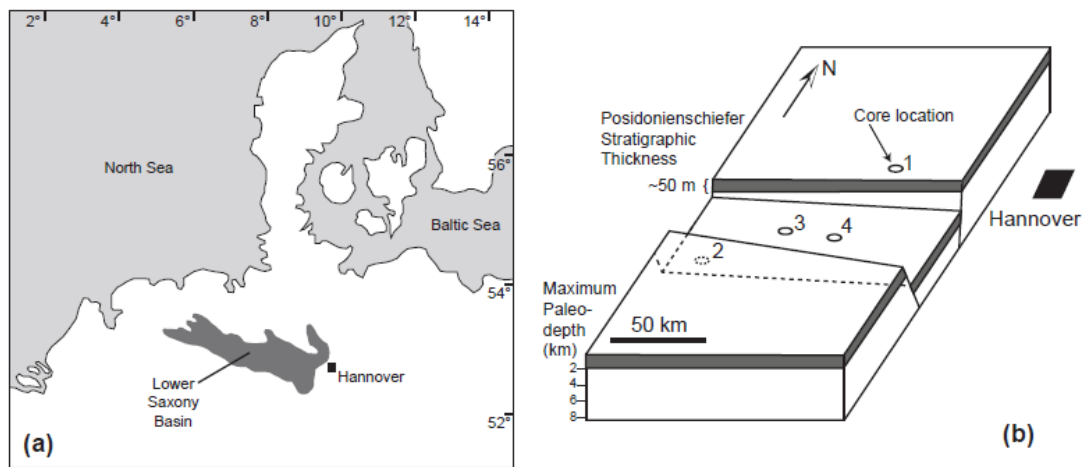
Figure 1. (a) Map of the study area, modified from Kockel et al., 1994. (b) Schematic block diagram showing locations of cores in this study and subsurface faults, synthesized from Baldschun et al. (1996). Shaded layer shows approximate maximum paleodepth of the top of the Posidonienschiefer (layer thickness exaggerated).
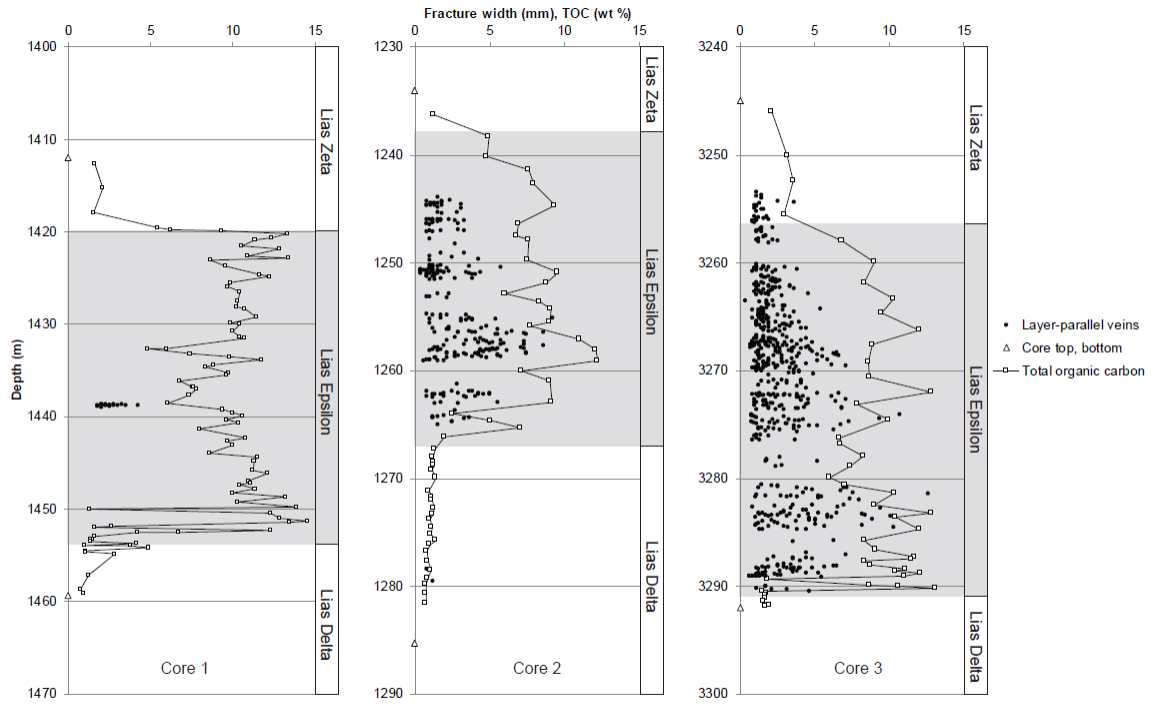
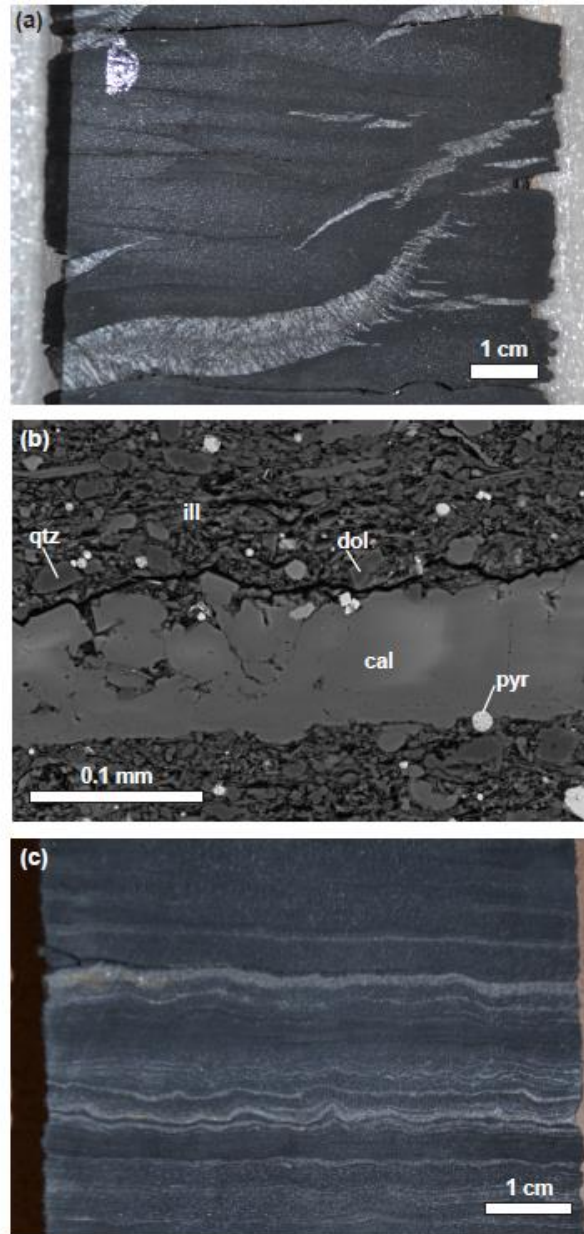**Figure 2.** Depths of layer-parallel, calcite-filled fractures and TOC versus depth, Cores 1 – 3.

Figure 3. (a) Photograph, Core 3, depth 3281 m. White calcite veins and uncemented cracks form at low angle to sedimentary layering. (b) Backscattered electron image, Core 3, depth 3280 m; cal: calcite; dol: dolomite; ill: illite; pyr: pyrite; qtz: quartz. Calcite grain is a ~50 micron thick overgrowth over a ~30 micron tall (thick) fossil, at the bottom. (c) Core 3, depth 3279 m. Laminated interval, showing mm-scale alternations of carbonate-rich (pale gray) and carbonate-poor (dark gray) intervals.
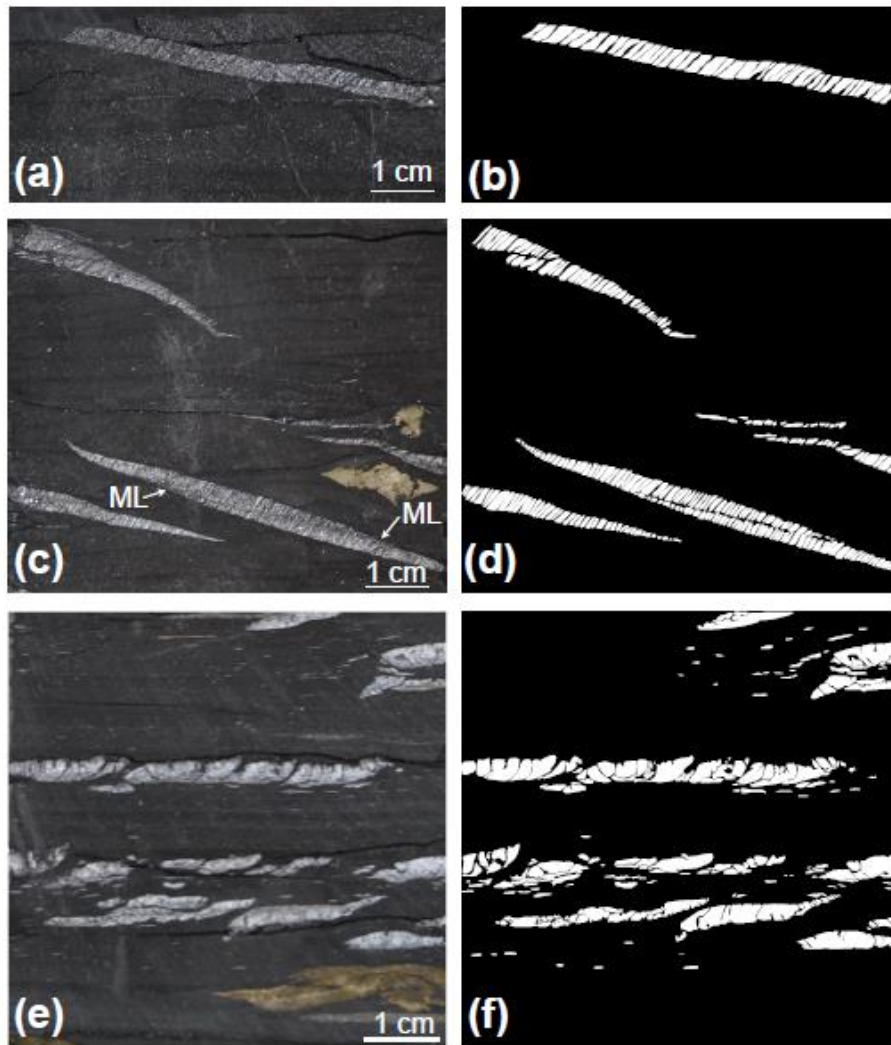
Figure 4. Photographs of layer-parallel fractures in cores. (a) Core 3, depth 3272 m. (b) Interpretation of (a). Calcite-filled veinlets in white. (c) Core 3, depth 3269 m. Note median line at an oblique angle to both bedding and vein walls. Pyrite cement has yellow hue. (d) Interpretation of geometries of calcite cements in (c). (e) Core 2, depth 1263 m. Core face is oblique to veinlets and roughly parallel to vein strike. Note pyrite in lower right. (f) Interpretation of geometries of calcite cements in (e).
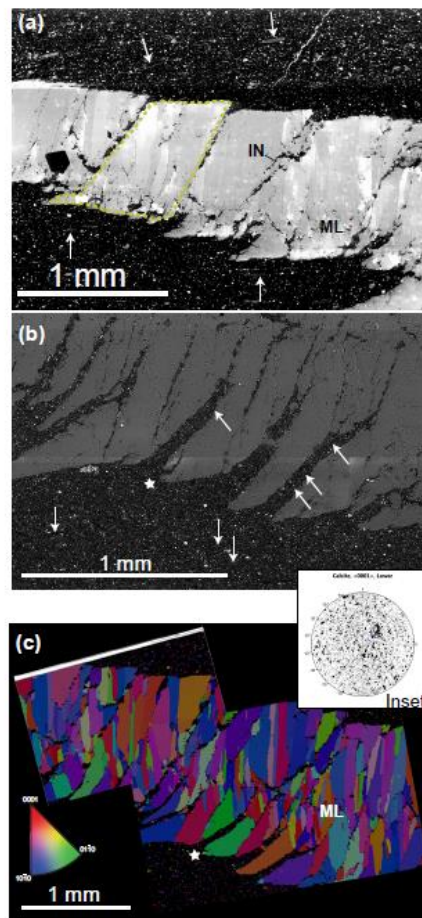
Figure 5. Layer-parallel veins, Core 3, depth 3267 m. (a) Monochromatic cathodoluminescence image. IN – host-rock inclusion. ML – median line. An individual veinlet is outlined by dashed green line. (b) Backscattered electron image. White arrows in (a) and (b) indicate detrital grains with long axes parallel to layering. Note grains within host-rock strands are rotated parallel to strands. (c) Electron backscatter diffraction map. Stars mark same location in (b) and (c). Pixel color corresponds to calcite crystallographic orientation, as shown in inverse pole figure (wedge diagram). Inset: Equal-area plot of calcite c-axes.
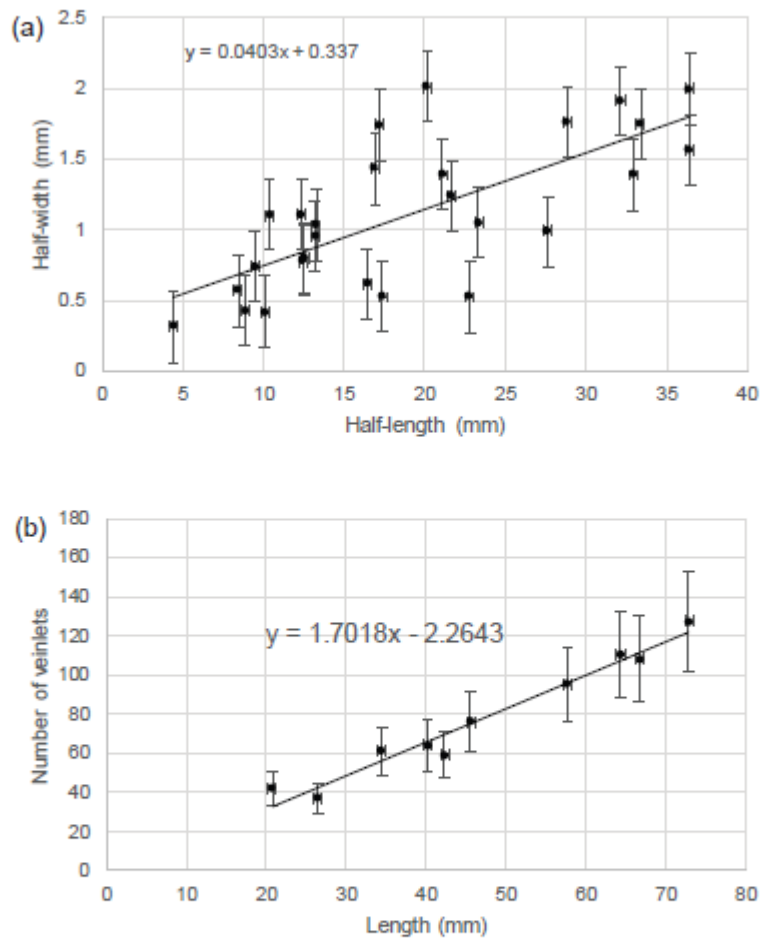
Figure 6. (a) Half-width versus half-length of layer-parallel calcite veins. (b) Number of veinlets versus total vein length. All measurements made at core scale.
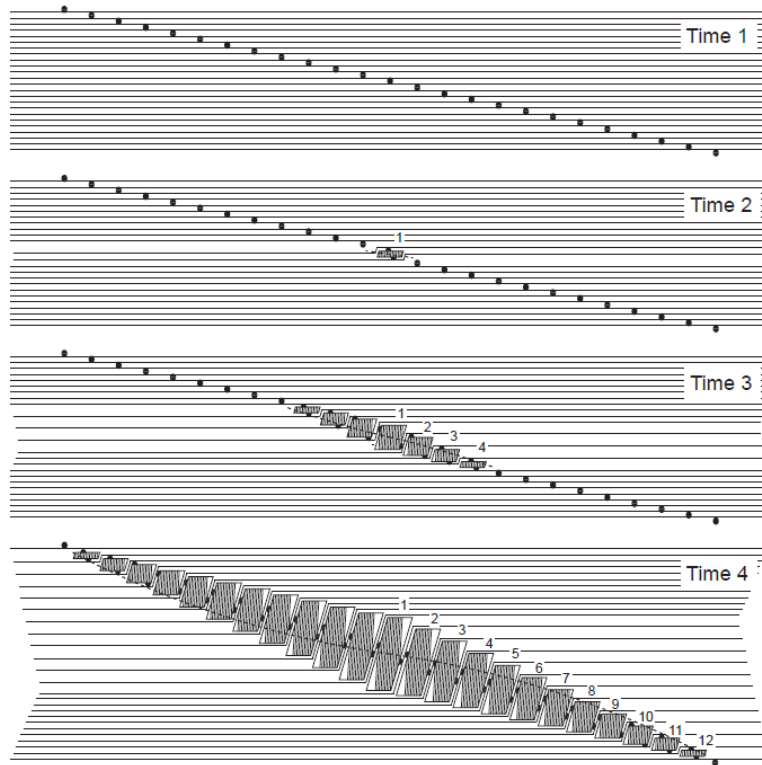
Figure 7. Schematic of a composite calcite vein from the Posidonienschiefer. Parallelograms are veinlets. Numbers show sequence of initiation of each veinlet, and vein growth is symmetrical; numbers omitted on top half for clarity. Striped areas within veinlets are fibrous; white areas are blocky (compare to Figure 5c). Median line is dashed. Black semicircles show offset of original circles before formation of veinlets. Thin horizontal lines represent bedding planes; regions of closely spaced bedding planes illustrate the original stratigraphic thickness, based on the assumption that that thickness is conserved within the (rotated) inclusions in between veinlets. Wide bedding plane spacing is drawn so that both the bedding line-lengths and the total host-rock area are conserved. The true strain distribution around veins is unclear and is likely compensated, at least in part, by neighboring veins.
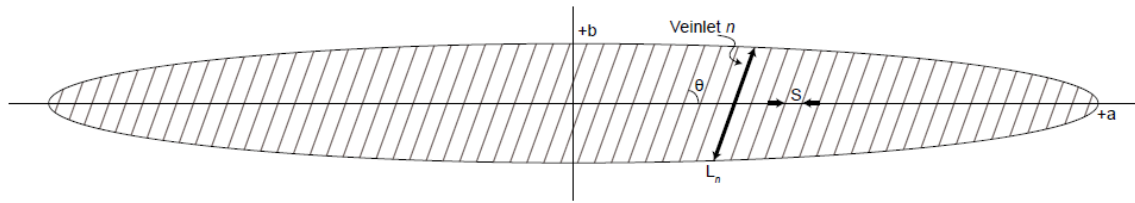
Figure 8. Representation of the surface area (per unit thickness into page) of an ideal, elliptical fracture versus that of an array of veinlets (parallel lines) that open along beddings planes and rotate the host rock to an angle θ with respect to the major axis. Variables from Equations 3 and 4 illustrated.
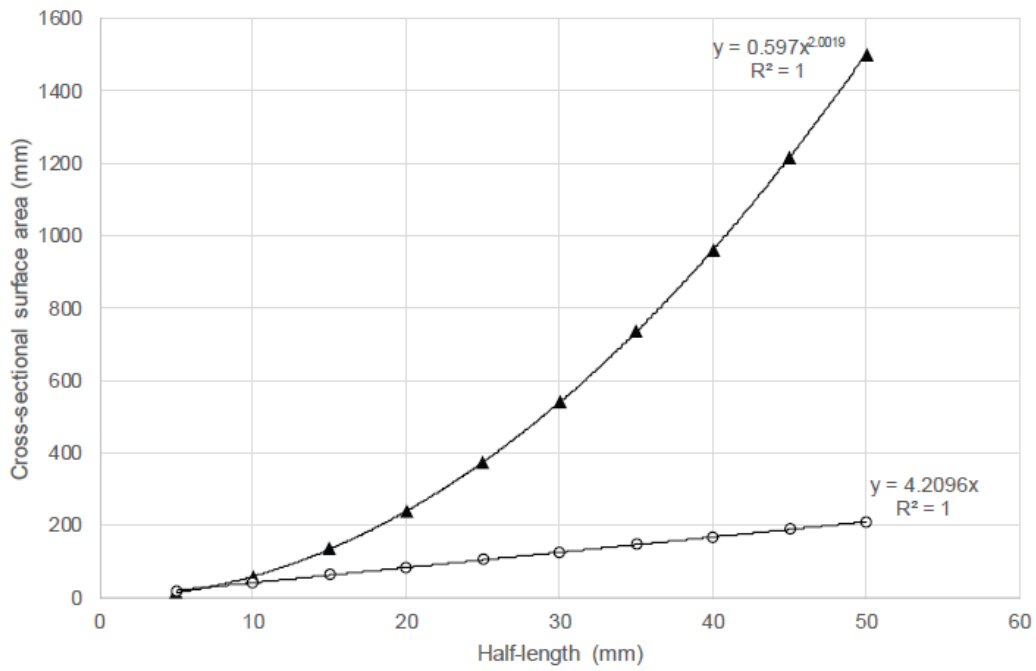
Figure 9. Increase in surface area, per unit thickness, with length, for an ellipsoidal crack (circles) and a vein comprising a series of veinlets (triangles). Note veinlet-array fracture surface area increases with the square of length, assuming linear aperture:length scaling.